ACS APPLIED OPTICAL MATERIALS



pubs.acs.org/acsaom

Article

# $Gd^{3+}$ and $Sm^{3+}$ Ions Modulated Visible-Light-Emitting ZnSe:$Mn^{2+}$ Nanocrystals for Detection of $Pb^{2+}$ and $Hg^{2+}$

Iram Gul, Zahid U. Khan,* Sammra Galani, Subul Huda, Latif U. Khan, Hassan K. Juwhari, Ali Hyder, Hermi F. Brito, Muhammad Zaheer, and Muhammad Abdullah Khan*

Cite This: *ACS Appl. Opt. Mater.* 2025, 3, 2067−2077

Read Online

ACCESS | Metrics & More | Article Recommendations | Supporting Information

**ABSTRACT:** Luminescent semiconductor nanocrystals (NCs) with strong visible emission are highly desirable for the sensitive detection of heavy metal ions at trace levels. Herein, the study focuses on enhanceing $Mn^{2+}$ ion emission achieved by incorporating trivalent lanthenide ($Ln^{3+}$) ions, *i.e.*, $Sm^{3+}$ and $Gd^{3+}$ ions, at the Zn sites in a ZnSe lattice. This enhancement was confirmed by integrated photoluminescence (PL) and X-ray emission optical luminescence (XEOL), supported by quantitative X-ray absorption fine structure (XAFS) analyses. The observed increase in the visible emission was attributed to efficient energy transfer from $Sm^{3+}$/$Gd^{3+}$ to $Mn^{2+}$ centers in ZnSe NCs. The luminescent NCs are subsequently employed as nanosensors for detecting $Pb^{2+}$ and $Hg^{2+}$ ions, exhibiting marked quenching upon exposure. The calculated limits of detection (LoDs) for $Pb^{2+}$ (2.51 $\mu$M) and $Hg^{2+}$ (6.63 $\mu$M) demonstrate greater sensitivity toward $Pb^{2+}$ as compared to $Hg^{2+}$. The system is selective across a range of interfering ions (i.e., $Ag^{1+}$, $Co^{2+}$, $Ni^{2+}$, $Cd^{2+}$, $Gd^{3+}$, $Tm^{3+}$, $Yb^{3+}$, and $Er^{3+}$) having different oxidation states when present concurrently. Furthermore, lifetime decay measurements, combined with Stern−Volmer analysis, indicate that quenching likely occurs through both static and dynamic mechanisms. These results highlight the potential of colloidal ZnSe:$Mn^{2+}$,$Sm^{3+}$ NCs as effective platforms for the sensitive and selective detection of toxic metal ions and have the potential to be employed for environmental monitoring applications.

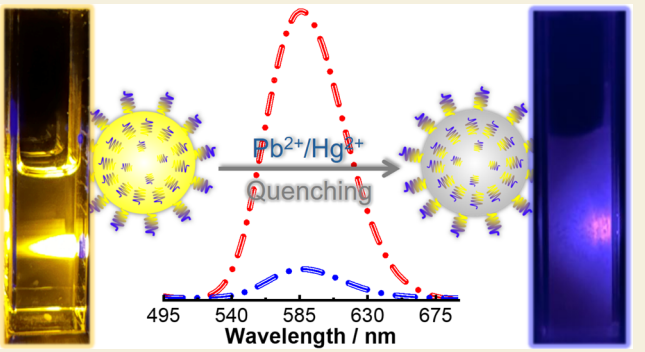


**KEYWORDS:** *Photoluminescent nanocrystals, Heavy metal ions detection, Lanthanide ions doping, Dynamic and static quenching, Colloidal nanosensors*



## 1. INTRODUCTION

Semiconductor nanocrystals (NCs) are luminescent nanoparticles that have emerged as promising candidates in various fields, including optoelectronics, quantum computing, photovoltaic cells, and biomedical applications.[1−4] They are considered intermediate species between atoms/molecules and bulk materials, exhibiting properties found either only in organic molecules or bulk inorganic materials.[5−9] Their key photoluminescent features arise from the radiative recombination of the exciton (photogenerated electron−hole pair) due to quantum confinement effects, particularly when the particle size is reduced to a length scale smaller than Bohr's radii.[7−9] However, recent developments have achieved color-tuning in semiconductor NCs without changing their size by various methods, including ion (cation/anion)-induced interfacial alloying, changing composition through gradient alloying, or the judicial incorporation of dopant impurities, i.e., d transition metals and lanthanide ions.[8,9]

The incorporation of dopant impurities in the NCs lattice offers the unique advantage of precisely adjusting their emissions within the desired spectral region.[2,7,10] This can be achieved by incorporating specific 3d transition metal ions, such as $Mn^{2+}$, or lanthanide ions, i.e., $Eu^{2+}$, $Eu^{3+}$, $Ce^{3+}$, and $Gd^{3+}$. Furthermore, the dopant impurities impart additional features to NCs, including stability, improved charge carrier dynamics, broadened absorption range, and magnetic behavior.[10−13] One specific example is the most widely investigated $Mn^{2+}$ ion-doped ZnSe matrix because of its unique optoelectronic properties.[8−10] They exhibit efficient visible emission at around 580 nm, corresponding to the $^4T_1 \rightarrow {}^6A_1$ transition of the $Mn^{2+}$ ions, which is characterized by a prolonged luminescence lifetime due to the spin-forbidden nature of this transition and the cubic symmetry of the structure.[13] As a result, ZnSe:$Mn^{2+}$ nanocrystals (NCs) were widely employed as optical markers for bioimaging,[14,15] dual-

Received: June 23, 2025
Revised: August 8, 2025
Accepted: August 11, 2025
Published: August 19, 2025

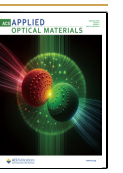

**Scheme 1. Overview of ZnSe:$Mn^{2+}$,$Ln^{3+}$ NCs Preparation, Their Aqueous Solubilization via Ligand Exchange, and Metal Ion Detection**

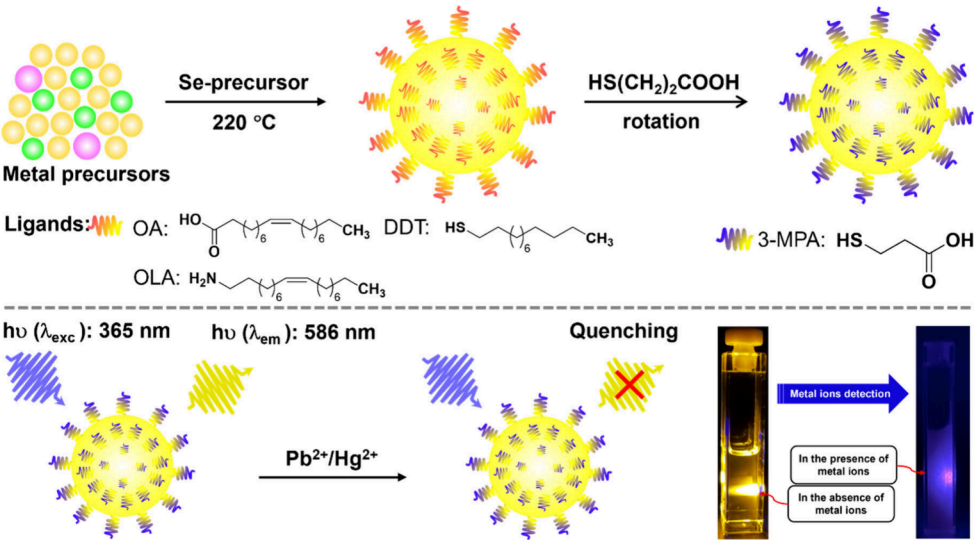


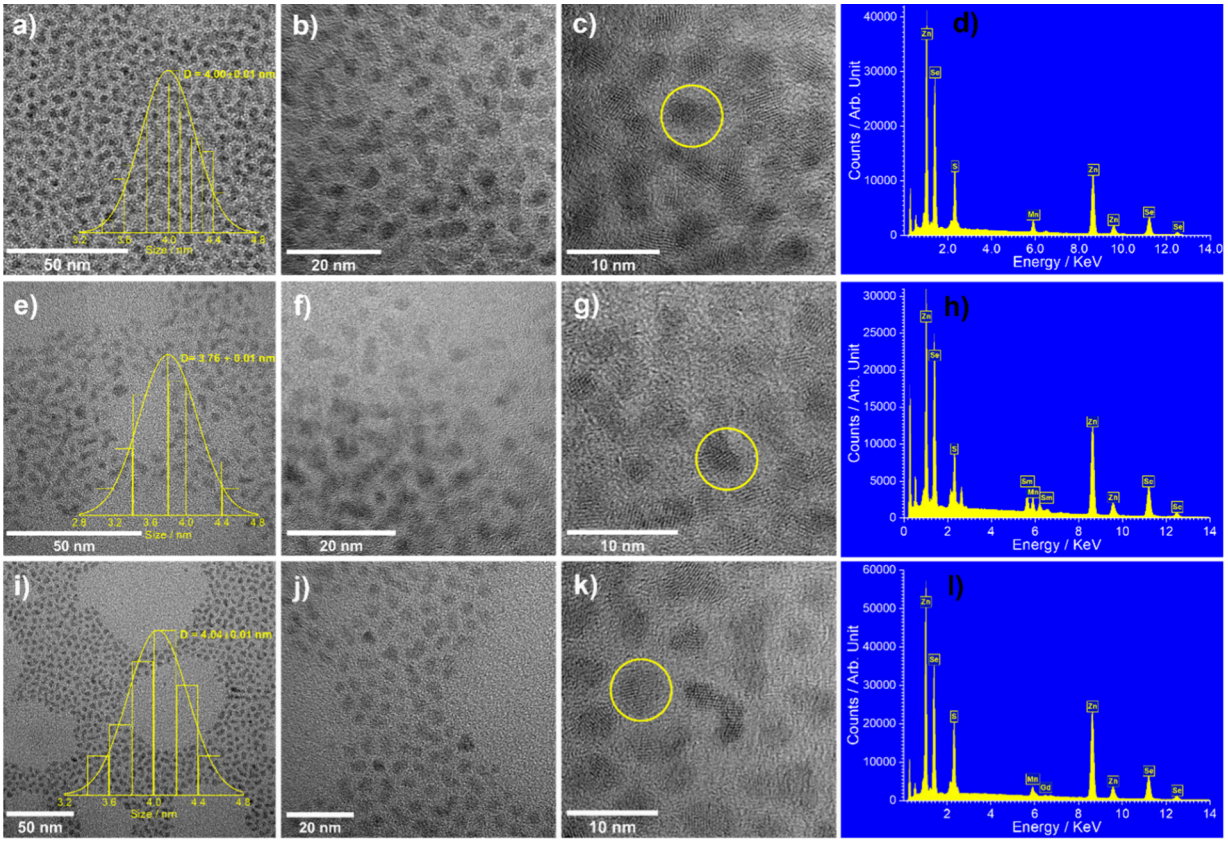


**Figure 1.** HRTEM images and the respective EDS spectra of ZnSe:$Mn^{2+}$ (a-d), ZnSe:$Mn^{2+}$,$Sm^{3+}$, (e-h), and ZnSe:$Mn^{2+}$,$Gd^{3+}$ NCs (i-l). The insets in (a,e,i) show the size distribution histogram of the corresponding NCs.

mode MRI/fluorescent imaging,[13] therapeutic applications,[16] biolabeling, and biosensing.[17] However, preparing highly photoluminescent ZnSe:$Mn^{2+}$ NCs is challenging due to their intrinsic self-purification during crystallization. They tend to expel impurities to the surface, where they possess incomplete valency and function as surface traps.[10,18] A strategy to address this is the doping of $Ln^{3+}$ ions in ZnSe:$Mn^{2+}$ that facilitates energy transfer to the $Mn^{2+}$ ions, thereby increasing the emitted light intensity and improving the sensing sensitivity.[10] Furthermore, $Ln^{3+}$ ions impart the system stability by protecting the $Mn^{2+}$ from oxidation, also improving its sensitivity toward interacting with specific heavy metal ions.

Heavy metal pollution in water involving toxic metals like mercury (Hg), lead (Pb), chromium (Cr), nickel (Ni), iron (Fe), and arsenic (As) poses significant risks to both humans and wildlife due to their persistence and bioaccumulation in aquatic systems.[19,20] These metal contaminants originate from


https://doi.org/10.1021/acsaom.5c00240
ACS Appl. Opt. Mater. 2025, 3, 2067−2077

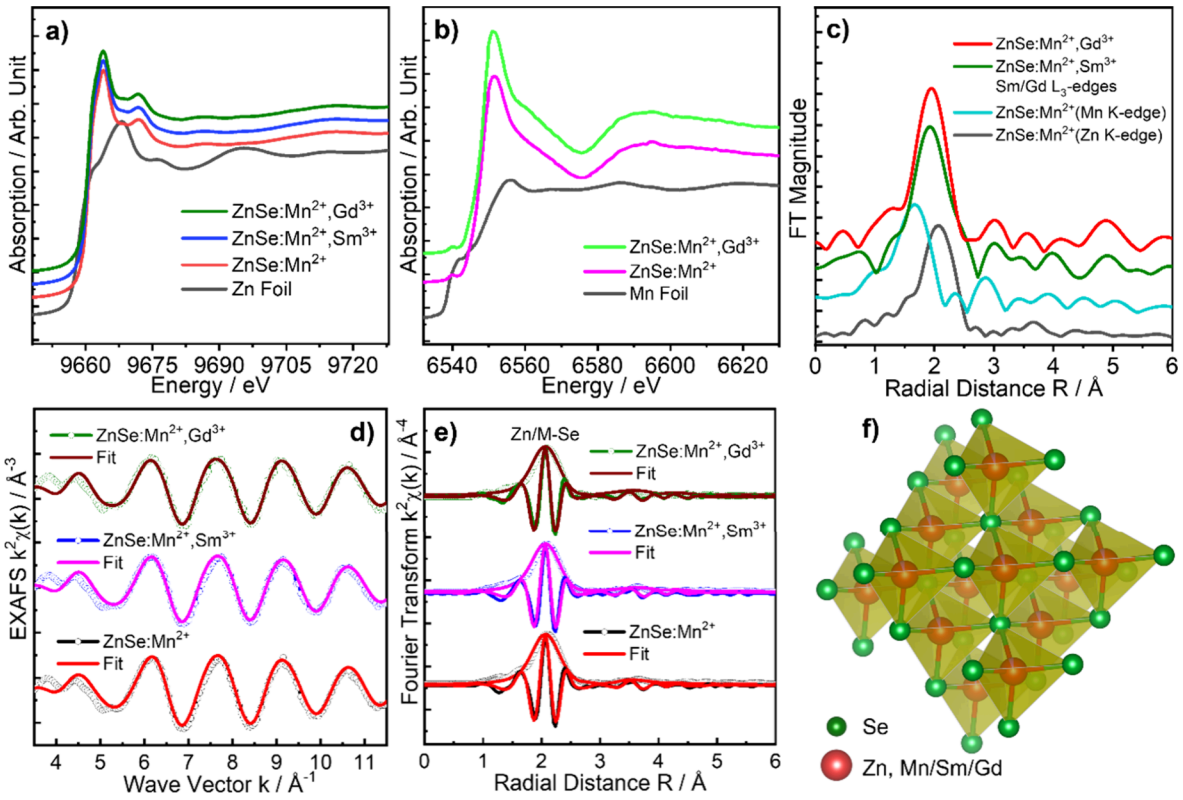


**Figure 2.** Normalized Zn *K*-edge (9659 eV) (a) and Mn *K*-edge (6539 eV) XANES spectra (b), Fourier transforms (FT) of Sm (6716 eV) and Gd (7243 eV) $L_3$-edge XAFS data (c), the $k^2$-weighted EXAFS signals (d), and the respective Fourier transforms (e) with best fits at the Zn K-edge, showing both the amplitude and the real parts of the Fourier transforms of $\chi(k)$ and fits for the $Gd^{3+}$- and $Sm^{3+}$-doped ZnSe:$Mn^{2+}$ NCs. The proposed three-dimensional crystallographic structure (f) of all of these nanocrystals.

industrial waste, mining, and agricultural runoff. Unlike organic pollutants, they do not degrade, leading to severe health issues even at low exposure levels.[21] Addressing this pollution is vital for water quality and public health. Quantum dot NCs, including ZnSe,[22] CdSe,[23] CdTe,[24] Mn-doped ZnS,[25] gold nanoparticles,[26] and Mn-doped ZnS or ZnSe,[27,28] along with graphene[29−31] and $MoS_2$,[5] have shown promising results in detecting trace metals through mechanisms like cation exchange and surface ligand interactions, exploiting their optical properties.[32] These nanosensors offer high sensitivity, low detection limits, and real-time monitoring, outperforming traditional methods in water contamination detection.[33] Due to their unique photoluminescence properties, $Mn^{2+}$-doped NCs have previously demonstrated potential for detecting toxic species, including Pb, Cu, Fe, Hg, and Cd metal ions.[34−37] These NCs offer a rapid, cost-effective, and sensitive detection method ideal for environmental monitoring.[38] Furthermore, their optical properties can be tailored to achieve detections of metal contaminants at ultratrace levels.

The study explores the enhancement of $Mn^{2+}$ emission intensity by doping with $Ln^{3+}$ ions ($Ln^{3+}$:$Sm^{3+}$ and $Gd^{3+}$) in the ZnSe NCs. The NCs were prepared by maintaining a fixed amount of $Mn^{2+}$ (7 mol %) while varying the concentration of $Sm^{3+}$ (2 to 10 mol %) and $Gd^{3+}$ (2 to 8 mol %) ions. The impact of $Ln^{3+}$ ions dopants on the $Mn^{2+}$ emission intensity was investigated by recording photoluminescent and XEOL spectra and analyzing the local environment of $Mn^{2+}$ ions by EXAFS. The ZnSe:$Mn^{2+}$,$Sm^{3+}$ NCs were subsequently used for the development of potential nanosensors for detecting heavy metal ions. The ZnSe:$Mn^{2+}$,$Sm^{3+}$ NCs demonstrated excellent selectivity and high sensitivity toward various metal ions, including $Pb^{2+}$ and $Hg^{2+}$ ions, indicating their potential for future development as a nanoprobe.

## 2. RESULTS AND DISCUSSION

The as-prepared NCs were soluble only in organic solvents; therefore, they were rendered water-soluble by treating with 3-mercaptopropionic acid (3-MPA) through a ligand exchange (Scheme 1) process following the previously reported procedure.[7,39] In this process, the thiol group (soft base) of 3-MPA binds onto the surface of NCs, forming Zn−S coordination bonds, while the carboxylate group (hard base) at the distal end of the ligand ensures compatibility with the aqueous medium.

X-ray diffraction (XRD) patterns of all the prepared NCs, including ZnSe:$Mn^{2+}$, ZnSe:$Mn^{2+}$,$Gd^{3+}$ and ZnSe:$Mn^{2+}$,$Sm^{3+}$ (Figure S1), exhibited three distinctive diffraction peaks at $2\theta$ values of 27.51, 45.93, and 54.06°, corresponding to the (111), (220), and (311) lattice planes of the cubic zinc-blende phase of ZnSe.[7,10] These peaks match reference ICDD/PDF 37-1463, confirming the formation of the ZnSe crystal structure. It is noteworthy that the incorporation of $Ln^{3+}$ ions in ZnSe:$Mn^{2+}$ did not result in a phase transition nor were any additional diffraction peaks related to $Ln^{3+}$ or $Ln_2Se_3$ phases detected compared to ZnSe:$Mn^{2+}$ NCs. The broadening of diffraction peaks in all of the XRD patterns suggests that the ZnSe:$Mn^{2+}$,$Ln^{3+}$ NCs exhibited small nanocrystalline structures.

The high resolution transmission electron microscopy (HRTEM) images of the ZnSe:$Mn^{2+}$,$Ln^{3+}$ (Figure 1) revealed


https://doi.org/10.1021/acsaom.5c00240
ACS Appl. Opt. Mater. 2025, 3, 2067−2077

Table 1. EXAFS Fitting for $Gd^{3+}$- and $Sm^{3+}$-Doped ZnSe:$Mn^{2+}$ NCs Includes *N*, *R*, $\sigma^2$ (MSRD/Debye-Waller Factor), $S_0^2$, $E_0$, and *R*-Factor for Structural Analysis

| Material | Bond Type | *N* | *R* (Å) | $\sigma^2$ (Å$^2$) | $S_0^2$ | $E_0$ (eV) | $R_{factor}$ |
|---|---|---|---|---|---|---|---|
| ZnSe:$Mn^{2+}$,$Gd^{3+}$ | $Zn_0$-$Se_1$ | 4 | 2.420 ± 0.008 | 0.0058 ± 0.0009 | 0.61 | 2.4 | 0.025 |
| | $Zn_0$-$Zn_1$ | 12 | 3.939 ± 0.096 | 0.0325 ± 0.0150 | 0.61 | 2.4 | 0.025 |
| | $Zn_0$-$Se_2$ | 12 | 4.610 ± 0.064 | 0.0227 ± 0.009 | 0.61 | 2.4 | 0.025 |
| ZnSe:$Mn^{2+}$,$Sm^{3+}$ | $Zn_0$-$Se_1$ | 4 | 2.418 ± 0.009 | 0.0063 ± 0.0010 | 0.64 | 2.3 | 0.027 |
| | $Zn_0$-$Zn_1$ | 12 | 3.962 ± 0.184 | 0.0384 ± 0.0184 | 0.64 | 2.3 | 0.027 |
| | $Zn_0$-$Se_2$ | 12 | 4.640 ± 0.077 | 0.0251 ± 0.0098 | 0.64 | 2.3 | 0.027 |
| ZnSe:$Mn^{2+}$ | $Zn_0$-$Se_1$ | 4 | 2.421 ± 0.008 | 0.0063 ± 0.0010 | 0.68 | 1.8 | 0.020 |
| | $Zn_0$-$Zn_1$ | 12 | 3.904 ± 0.252 | 0.0314 ± 0.0033 | 0.68 | 1.8 | 0.020 |
| | $Zn_0$-$Se_2$ | 12 | 4.506 ± 0.074 | 0.0299 ± 0.0074 | 0.68 | 1.8 | 0.020 |

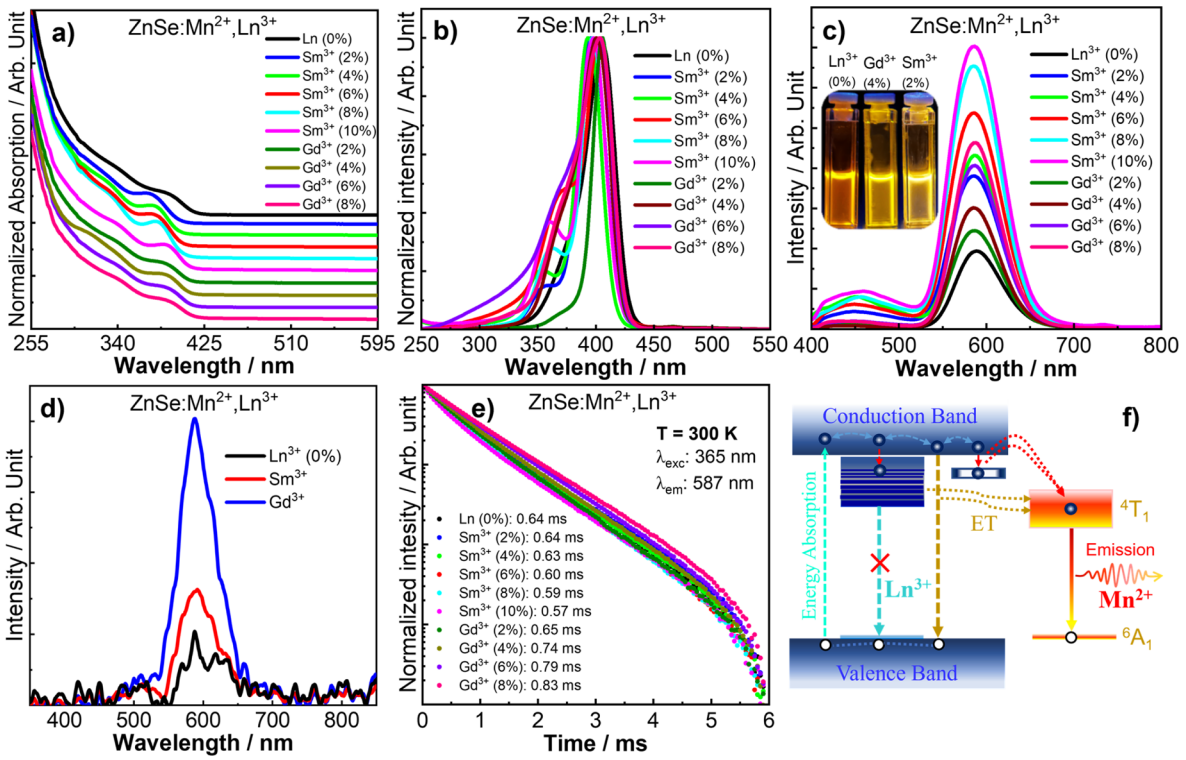


**Figure 3.** (a) Absorption spectra, (b) excitation spectra, (c) and emission spectra of ZnSe:$Mn^{2+}$,$Ln^{3+}$ doped with varying amounts of $Sm^{3+}$ (2, 4, 6, 8, and 10 mol %) and $Gd^{3+}$ (2, 4, 6, and 8 mol %), as well as (d) X-ray excited optical luminescence spectra of ZnSe:$Mn^{2+}$,$Ln^{3+}$ ($Ln^{3+}$:$Sm^{3+}$ and $Gd^{3+}$, 2 mol %) NCs. (e) Decay curves of ZnSe:$Mn^{2+}$,$Sm^{3+}$ and ZnSe:$Mn^{2+}$,$Gd^{3+}$ NCs, at varying concentrations, recorded under excitation at 365 nm while monitoring the emission at 586 nm ($Mn^{2+}$, $^4T_1 \rightarrow {}^6A_1$). (f) A partial energy level diagram with red arrows shows energy transfer, and blue and yellow downward arrows indicate radiative decay from the band gap and $Mn^{2+}$ ions, respectively.

ultrasmall NCs elliptical or slightly round in shape, displaying a narrow size distribution. The dominant average diameter of the ZnSe:$Mn^{2+}$, ZnSe:$Mn^{2+}$,$Sm^{3+}$, and ZnSe:$Mn^{2+}$,$Gd^{3+}$ NCs was determined to be approximately 4.00 ± 0.01, 3.76 ± 0.01, and 4.04 ± 0.01 nm, as deduced from the particle size distribution histogram (Figure 1a-h). This average size was determined using ImageJ software with nonlinear curve fitting (Gauss fit) conducted in Origin 8.5. The composition of ZnSe:$Mn^{2+}$, ZnSe:$Mn^{2+}$,$Sm^{3+}$, and ZnSe:$Mn^{2+}$,$Gd^{3+}$ NCs was validated by performing EDS analysis (Figure 1d,h,i).

### 2.1. Probing Local Atomic Structure Order of ZnSe:$Mn^{2+}$,$Ln^{3+}$ NCs by XAFS

The Zn K-edge XANES spectra (Figure 2a) of the $Sm^{3+}$- and $Gd^{3+}$-doped ZnSe:$Mn^{2+}$ NCs displayed a typical sharp absorption edge peak at ~9661 eV, followed by a smaller peak in the region of 50 eV above the edge, characteristic of the Zn *K*-absorption edge in the selenide lattice. The appearance of identical near-edge features for the $Sm^{3+}$- and $Gd^{3+}$-doped ZnSe:$Mn^{2+}$ NCs manifested an isostructural local coordination environment around the $Zn^{2+}$ site. Notably, the distinct shape of $Zn^{2+}$ cation *K*-edge XANES and the respective energy distribution of the p-like densities of states are mainly determined by the type of counteranion, for instance, Se and S in ZnSe and ZnS materials, respectively. The *K*-edge of Zn in sulfides usually exhibits three well-defined peaks until 50 eV above the edge, while selenide analogs exhibit only two prominent peaks. Therefore, the presence of two distinct peaks in the near-edge spectral region (Figure 2a) demonstrated the existence of the ZnSe lattice for the $Ln^{3+}$- and $Mn^{2+}$-doped ZnSe NCs. In addition, the Mn K-edge XANES spectra of these NCs also exhibited the existence of Mn in the +2-oxidation state (Figure 2b), whereas the similar near-edge features for the $Ln^{3+}$-doped ZnSe:$Mn^{2+}$ when compared to the ZnSe:$Mn^{2+}$ NCs (Figure 2b) also displayed


https://doi.org/10.1021/acsaom.5c00240
ACS Appl. Opt. Mater. 2025, 3, 2067−2077

a similar local chemical environment for the Mn site. Additionally, the Fourier transform (FT) of the Sm/Gd $L_3$-edge and Mn *K*-edge EXAFS data (Figure 2e) demonstrated that the trivalent rare earth and divalent Mn ions occupy the Zn site in the ZnSe lattice. Though the slight shift in the position of the first peak from the nearest Se backscatters for the Gd and Sm $L_3$-edges XAFS data (Figure 2c) when compared to the corresponding peak of the host Zn and Mn K-edges ones is attributed to the variation in the ionic radii of the trivalent gadolinium and samarium ions (Figure S2).

**Quantitative EXAFS Analysis.** The comprehensive insight into the local atomic structure order of the $Sm^{3+}$- and $Gd^{3+}$-doped ZnSe:$Mn^{2+}$ NCs was unraveled by a quantitative nonlinear fit to their Zn *K*-edge (9659 eV) extended X-ray absorption fine structure (EXAFS) data, using the Larix (XrayLarch) package.[40] The XAFS data were normalized and preprocessed before quantitative fit using Athena from Demeter, according to the previously reported procedure.[41] The nonlinear fit to the experimental $\chi(k)$ was performed in R-space, using a literature reported zinc blende crystal structure of the ZnSe:$Mn^{2+}$ with lattice parameters $a = b = c = 5.687$ Å, and a space group of $F43m$ (216) to derive the effective backscattering amplitudes and phase shifts, using feff8-lite code implemented in XrayLArch,[40] thereby generating various scattering paths.[41] The experimental EXAFS data in R-space from 1.0 to 4.65 Å with a Hanning window and *k* range of 3−12 $Å^{-1}$ were used in the best-fit analyses. The initial three high-ranking single scattering paths of $Zn_0$-$Se_1$, $Zn_0$-$Zn_1$, and $Zn_0$-$Se_2$ bond pairs were included in the fit. The passive electron reduction factor $S_0^2$ and energy shift $E_0$ were set similarly for all the paths in the fit of all the NCs, whereas the mean-square relative displacement $\sigma^2$ and interatomic distance *R* were refined relatively to get the best-fit result.

The quantitative Zn *K*-edge EXAFS analyses manifested similar experimental and theoretical $k^2$-weighted EXAFS signals (Figure 2d), indicating a similar local structure for the $Sm^{3+}$- and $Gd^{3+}$-doped ZnSe:$Mn^{2+}$ NCs. The Fourier transform (FT) of the Zn *K*-edge EXAFS data (Figure 2e) displayed the first dominant peak associated with the nearest Se neighboring atoms. The best-fit result exhibited four backscattering Se atoms (Table 1), comprising the first coordination shell around the Zn photoabsorber, corresponding to the cubic zinc blende local crystal lattice of ZnSe for both the NCs. It is noteworthy that the position of the first coordination shell peak was found to be slightly asymmetric and shifted toward lower interatomic distance R when compared to ZnSe:$Mn^{2+}$ (Table 1), owing to the contribution from a change in the photoelectron phase shift,[10] caused by codoping of $Sm^{3+}$ and $Gd^{3+}$, with different ionic radii, in the ZnSe:$Mn^{2+}$ lattice at the Zn site. This is also caused by structural disorder/defects and distortion in the lattice, as demonstrated by higher mean square relative displacements (MSRDs) or Debye−Waller factor ($\sigma^2$) values for the $Ln^{3+}$-doped ZnSe:$Mn^{2+}$ NCs (Table 1). Nevertheless, the detailed XAFS data analysis manifested that the trivalent lanthanide ions occupy the Zn site in the ZnSe:$Mn^{2+}$ lattice.

## 2.2. Photoluminescent Study

The UV−visible absorption spectrum of ZnSe:$Mn^{2+}$ NCs exhibited the first excitonic absorption band around 392 nm. Upon doping with $Ln^{3+}$ ions (2% each), a slight blue shift was observed in the absorption spectra of ZnSe:$Mn^{2+}$,$Sm^{3+}$ and ZnSe:$Mn^{2+}$,$Gd^{3+}$, with shifts of 71 and 388 nm, respectively (Figure 3a), suggesting a quantum confinement effect. However, as the amount of $Sm^{3+}$ and $Gd^{3+}$ ions increased, the absorption spectra of NCs exhibited a gradual red shift compared to those of lower doping levels. These alterations in the absorption maxima can likely arise from lattice strain and contraction induced by the mismatch of ionic size and charge differences between the dopants ($Sm^{3+}$/$Gd^{3+}$) and host matrix ions. The excitation spectra of ZnSe:$Mn^{2+}$,$Sm^{3+}$ and ZnSe:$Mn^{2+}$,$Gd^{3+}$ (Figure 3b) NCs, monitored at ∼586 nm ($Mn^{2+4}T_1(^4G) \rightarrow {}^6A_1(^6S)$), also exhibited a slight blue shift in the main excitation peak relative to undoped ZnSe:$Mn^{2+}$ NCs. These observations are consistent with trends seen in UV−visible absorption spectra, further supporting the dopant-induced alteration in the electronic structure of NCs. The emission spectrum of ZnSe:$Mn^{2+}$ (Figure 3c) displayed an emission band assigned to the spin-forbidden intraconfigurational $3d^5$ transition of tetrahedrally coordinated $Mn^{2+}$ ions. Interestingly, $Mn^{2+}$ emission intensity exhibited systematic enhancement as the dopant concentration of $Sm^{3+}$ or $Gd^{3+}$ ions was gradually increased from 2 to 8% and 2 to 10 mol %, respectively, while the concentration of $Mn^{2+}$ was maintained to be constant in ZnSe NCs. However, the emission intensity exhibited an irregular trend with increasing $Sm^{3+}$ and $Gd^{3+}$ concentrations, likely due to modified energy transfer processes from codopants with additional contributions from defect-mediated energy transfer,[42] arising from local structure distortions caused by ionic radii mismatch. The enhancement in emission intensity was markedly stronger for $Sm^{3+}$ doping than for $Gd^{3+}$ ions at an equivalent concentration. Furthermore, increasing the amount of $Gd^{3+}$ ions led to earlier onset of quenching at 8 mol%, whereas $Sm^{3+}$ ions continued to enhance the emission intensity up to 10 mol%. These variations may likely have originated from differences in ionic radii of $Sm^{3+}$/$Gd^{3+}$ ions, inducing different lattice strain, and differences in energy transfer efficiency between $Sm^{3+}$/$Gd^{3+}$ and the $Mn^{2+}$ centers. It is noteworthy that $Sm^{3+}$ ions possess a more favorable energy structure for efficient energy transfer to $Mn^{2+}$ as compared to the energy level of $Gd^{3+}$ ions, which may not align well with the band gap of ZnSe and subsequent energy transfer to $Mn^{2+}$ ions. Additionally, $Sm^{3+}$ ions have a higher absorption cross-section, improving their ability to absorb photons and transfer them to $Mn^{2+}$ ions. Among the previously screened $Ln^{3+}$ ions ($Ln^{3+}$:$La^{3+}$, $Y^{3+}$, $Nd^{3+}$, $Yb^{3+}$, $Tm^{3+}$, $Lu^{3+}$, and $Eu^{3+}$)[10,42] in ZnSe:$Mn^{2+}$ NCs, $Sm^{3+}$ was identified as the most effective sensitizer, enhancing the emission of $Mn^{2+}$ centers by 3.63-fold. Similarly, the codoping of $Gd^{3+}$ into ZnSe:$Mn^{2+}$ resulted in a 2.39-fold increase in the emission intensity of the $Mn^{2+}$ centers. The observed enhancement was previously attributed to energy transfer from the $Ln^{3+}$ ions, accompanied by defects, created due to the mismatch in ionic radii and oxidation states between Zn and Ln.[10,42]

The energy transfer from $Ln^{3+}$ to $Mn^{2+}$ ions was further validated by performing X-ray excited optical luminescence (XEOL) measurements (Figure 3d), conducted under monochromatic X-ray excitation at the Zn *K*-edge absorption region (9.75 keV), above the Gd and Sm $L_{1,2,3}$-edges. Upon X-ray irradiation, ZnSe:$Mn^{2+}$ exhibited weak orange emission from the ${}^4T_1 \rightarrow {}^6A_1$ transition of $Mn^{2+}$ ions. However, incorporating $Ln^{3+}$ ions at the Zn site in the lattice led to a marked increase in the orange emission in ZnSe:$Mn^{2+}$,$Sm^{3+}$ and ZnSe:$Mn^{2+}$,$Gd^{3+}$ NCs. The ZnSe:$Mn^{2+}$,$Sm^{3+}$ exhibited a weaker emission intensity compared to ZnSe:$Mn^{2+}$,$Gd^{3+}$ NCs.


https://doi.org/10.1021/acsaom.5c00240
ACS Appl. Opt. Mater. 2025, 3, 2067−2077

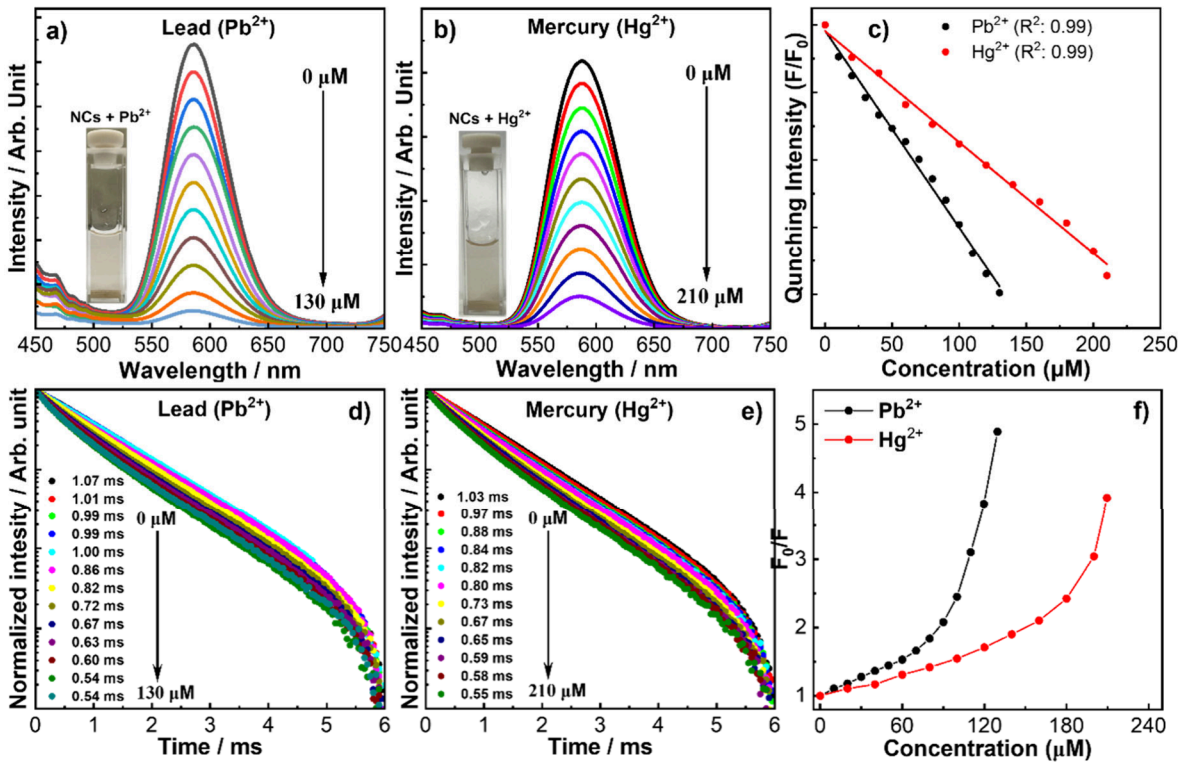


**Figure 4.** (a) Overview of photoluminescent quenching spectra of ZnSe:$Mn^{2+}$,$Sm^{3+}$ NCs recorded upon addition of increasing amounts of (a) $Pb^{2+}$ and (b) $Hg^{2+}$, and the (c) corresponding plot for decrease in emission intensity with increasing quencher concentration. Lifetime decay curves in the presence of varying amounts of (d) $Pb^{2+}$ and (e) $Hg^{2+}$ and (f) Stern−Volmer plot.

This optical result is because X-ray irradiation produces a large number of photogenerated electron−hole pairs through the photoelectric effect, Auger process, and ionization.[43] Some electron−hole pairs form excitons via Coulomb interactions, which recombine and transfer the energy to $Gd^{3+}$ and $Sm^{3+}$. Hence, the relaxation of $Gd^{3+}$ led to an increased population of $Mn^{2+}$ due to possessing a higher energy structure for efficient energy transfer to $Mn^{2+}$ than $Sm^{3+}$, which involves lower energy transitions.

The PL decay curves (Figure 3e) revealed distinct dopant-specific effects on the $Mn^{2+}$ emission dynamics. In ZnSe:$Mn^{2+}$,$Sm^{3+}$, the lifetime systematically decreased from 0.64 to 0.57 ms with increasing $Sm^{3+}$ concentration, indicating the introduction of competing nonradiative decay pathways through the incorporation of $Sm^{3+}$ in addition to improved energy absorption (possibly via $Sm^{3+}$ sensitization). Nevertheless, the lifetime of ZnSe:$Mn^{2+}$,$Sm^{3+}$ NCs increased to 1.07 ms (Figure 4d) following ligand exchange with 3-MPA, likely due to the suppression of surface-related quenching. In contrast, ZnSe:$Mn^{2+}$,$Gd^{3+}$ displayed lifetime enhancement from 0.65 to 0.83 ms at higher $Gd^{3+}$ doping levels, which suggests the suppression of competing relaxation channels as well as energy transfer to $Mn^{2+}$ centers.

## 2.3. Heavy Metal Ion Detection

The potentials of ZnSe:$Mn^{2+}$,$Sm^{3+}$, NCs were systematically evaluated for sensing toxic heavy metals ions, including $Pb^{2+}$ and $Hg^{2+}$. Metal ions are known to interact with NCs, thereby quenching their photoluminescence properties through various mechanisms: fluorescence resonance energy transfer (FRET), electron transfer, static quenching, dynamic quenching, or competitive cation exchange processes, etc.[44−47] Therefore, the detection was achieved by monitoring the PL spectra (Figure 4a,b), relative emission quenching ($F/F_0$, Figure 4c), and lifetime decay profile (Figure 4d,e) of NCs in the presence of $Pb^{2+}$ and $Hg^{2+}$, respectively. The introduction of $Pb^{2+}$ or $Hg^{2+}$ into an NCs dispersion caused significant quenching of PL (Figure 4a,b) for both ions. Furthermore, the PL intensity exhibited a concentration-dependent decrease with increasing concentration of either ion: $Pb^{2+}$ (from 1 to 130 $\mu$M) or $Hg^{2+}$ (from 1 to 210 $\mu$M) (Video S1). These findings suggest that either ion incorporated nonradiative recombination processes, disrupting the radiative recombination of charge carriers within the NCs. Moreover, the NCs dispersion was rendered slightly turbid, likely due to its aggregation. Previous studies have shown that $Pb^{2+}$ and $Hg^{2+}$ ions exhibit a strong affinity for thiol groups, which can promote ligand detachment from the NCs' surface, thereby leading to their aggregation.[45,48−50]

A comparative analysis of $Pb^{2+}$ and $Hg^{2+}$ detection performance by ZnSe:$Mn^{2+}$,$Sm^{3+}$, relative to previous studies, is presented in Table 2.

The quenching effect of $Pb^{2+}$ and $Hg^{2+}$ on NCs was further quantitatively analyzed using the Stern−Volmer equation[57] (Equation S1). The luminescent ratios ($F/F_0$) were decreased progressively with increasing the amount of either $Pb^{2+}$ or $Hg^{2+}$ (Figure 4c), following a linear Stern−Volmer relationship between ($F_0/F$)−1 and quencher concentration (Figure 4f). These findings suggest that a higher quencher concentration results in more effective suppression of PL behavior, leading to significantly lower emission intensity. However, the nanosensor system was observed to demonstrate higher sensitivity toward $Pb^{2+}$ ions ($K_{sv}$ = 0.2074 $\mu M^{-1}$, LoD = 2.51 $\mu$M), compared to $Hg^{2+}$ ($K_{sv}$ = 0.0266 $\mu M^{-1}$, LoD = 6.63 $\mu$M), as quantified by the Stern−Volmer plot and limit of detection (LoD) calculations (Equation S2).[34] Furthermore, the


https://doi.org/10.1021/acsaom.5c00240
ACS Appl. Opt. Mater. 2025, 3, 2067−2077

**Table 2. Photoluminescent Probes Reported for $Pb^{2+}$ and $Hg^{2+}$ Ion Detection**

| Metals | Materials | Mechanism | Linear Range | LoD | refs. |
|---|---|---|---|---|---|
| $Pb^{2+}$ | ZnSeS/Cu:ZnS/ZnS | PL quenching | 0–20 $\mu$M | 28 nM | 33 |
| | $AgInS_2$ | Fluorescence quenching | 530 nM | 4n M | 51 |
| | ZnSe:$Mn^{2+}$ | PL quenching | 0–100 $\mu$M | 29.8 × $10^{-6}$ mol $L^{-1}$ | 34 |
| | ZnSe | Fluorescence quenching | 1–60 $\mu$g $L^{-1}$ | 0.335 $\mu$g $L^{-1}$ | 52 |
| | CdS | Off fluorescence | 20–60 $\mu$M | 60 nM | 53 |
| | ZnSe:$Mn^{2+}$,$Sm^{3+}$ | PL quenching | 0–130 $\mu$M | 2.51 $\mu$M | This work |
| $Hg^{2+}$ | TGA-CdTe/CdS/ZnS | Fluorescence quenching | 20–70 nM | 16.32 nM | 49 |
| | Mn-ZnSe | Fluorometric | 30 × $10^{-6}$ $mL^{-1}$ | 6.63 × $10^{-7}$ $mL^{-1}$ | 50 |
| | MSA-CdTe | Turn-On | 0.2–6 $\mu$M | 0.05 $\mu$M | 54 |
| | CdS/ZnS | Turn-Off | 0.1–3.5 $\mu$M | 0.09 $\mu$M | 55 |
| | ZnS:Ce | Ratiometric | 10–100 $\mu$M | 0.82 $\mu$M | 56 |
| | ZnSe:$Mn^{2+}$,$Sm^{3+}$ | PL quenching | 0–210 $\mu$M | 6.63 $\mu$M | This work |

quenching efficiencies calculated via Equation S3[34] revealed stronger suppression for $Pb^{2+}$ (80%) than $Hg^{2+}$ (75%), with $Pb^{2+}$ achieving photoluminescence quenching at a lower concentration.

To evaluate whether nanosensors can discriminate among other metals, a range of metal ions, including $Ag^{1+}$, $Co^{2+}$, $Ni^{2+}$, $Cd^{2+}$, $Gd^{3+}$, $Tm^{3+}$, $Yb^{3+}$, and $Er^{3+}$, were tested. The addition of ions such as $Co^{2+}$ and $Ag^{+}$ (Figure S4) led to a slight enhancement in emission intensity, possibly due to the passivation of surface traps by these ions.[45] In contrast, the introduction of $Ni^{2+}$, $Cd^{2+}$, $Gd^{3+}$, $Tm^{3+}$, $Yb^{3+}$, and $Er^{3+}$ ions resulted in minimal or negligible quenching effects (Figure S4). Although the nanosensors showed high sensitivity for both $Pb^{2+}$ and $Hg^{2+}$ individually, they lacked selective discrimination between these ions when they were present simultaneously in mixed solutions. It is because the observed quenching response demonstrated combined contributions from both $Pb^{2+}$ and $Hg^{2+}$ ions in solution rather than distinct quenching from either ion individually (Figure S5). Given the potential cross-sensitivity of nanosensors to various metal ions, we systematically investigated interference effects from $Cd^{2+}$, $Co^{2+}$, $Ni^{2+}$, and $Ln^{3+}$ ($Gd^{3+}$ and $Tm^{3+}$) across a broad concentration range, along with $Pb^{2+}$ or $Hg^{2+}$ ions in solutions. Increasing the concentration of $Cd^{2+}$, $Co^{2+}$, and $Ni^{2+}$ ions produced largely no quenching effect (Figure S6) and negligible interaction. In contrast, a significant decrease in emission intensity was observed upon increasing the concentration of $Pb^{2+}$ or $Hg^{2+}$ ions. Furthermore, tests with $Ln^{3+}$ ($Gd^{3+}$ and $Tm^{3+}$) induced marginal concentration-dependent luminescence suppression (Figure S7), highlighting the preferential response of the nanosensors to $Pb^{2+}$ and $Hg^{2+}$. Overall, this NC sensor with detection capabilities down to micromolar concentrations and high selectivity over other metal ions has great potential for environmental monitoring applications

## 2.4. Mechanism Proposal

Based on the data collected in this work, a reaction pathway for PL quenching and the detection of heavy metals is proposed. In ZnSe:$Mn^{2+}$,$Sm^{3+}$ nanosensors, the significant reduction in photoluminescence lifetime from ~1.07 to 0.54 ms for $Pb^{2+}$ (Figure 4d) and 1.03 to 0.55 ms for $Hg^{2+}$ (Figure 4e) indicates dynamic quenching (Figure 5), where these heavy metal ions are likely to quench $Mn^{2+}$ emission through energy/charge transfer during the excited state. Such dynamic quenching occurs when a quencher interacts with the fluorophore in its excited state, leading to nonradiative deactivation through processes like energy or electron transfer, which shortens the photoluminescence lifetime.[43,44] This is further supported by the Stern–Volmer plot (Figure 4f). As in dynamic quenching, the linear S–V relationship shows deviations at higher concentrations owing to underlying competing processes.[34,51]

Further, the upward tilt of the S–V plot suggests the presence of likely static quenching, as $Pb^{2+}$ and $Hg^{2+}$ ions could bind to the NCs' surface in the ground state, forming nonluminescent complexes and reducing the number of emissive $Mn^{2+}$ centers (Figure 5). Since static quenching does not alter the lifetime of the remaining unbound NCs, the observed lifetime reduction is primarily driven by the dynamic process, while intensity loss stems from both mechanisms.[12] Overall, the combined action of dynamic and static quenching

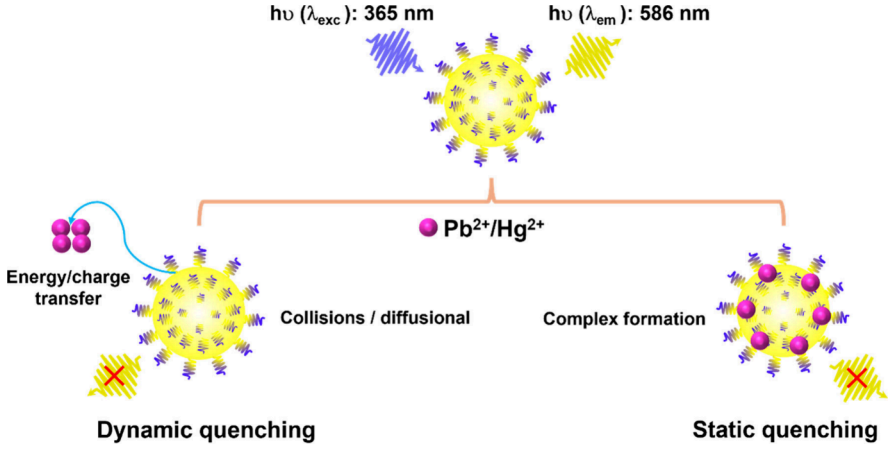


**Figure 5.** Proposed mechanism of ZnSe:$Mn^{2+}$,$Sm^{3+}$ NCs quenching by $Pb^{2+}$ and $Hg^{2+}$ ions. Both the dynamic (collisional) and static (complexation-mediated) quenching pathways were evaluated through Stern–Volmer plots and lifetime reduction.



https://doi.org/10.1021/acsaom.5c00240
ACS Appl. Opt. Mater. 2025, 3, 2067–2077

mechanisms explains the observed nonlinear S−V behavior and the reduction in lifetimes, highlighting the dual role of $Pb^{2+}$ and $Hg^{2+}$ in both excited-state deactivation and ground-state complexation with ZnSe:$Mn^{2+}$,$Sm^{3+}$ NCs.

## 3. CONCLUSION

In summary, we showed a strategy to successfully enhance the PL properties of ZnSe:$Mn^{2+}$ NCs through codoping with trivalent lanthanide ions, $Sm^{3+}$ and $Gd^{3+}$. The incorporation of $Ln^{3+}$ ions at $Zn^{2+}$ sites facilitated efficient energy transfer to $Mn^{2+}$ centers, which resulted in significantly enhanced emission, as confirmed by XEOL, lifetime decay, and EXAFS analyses. Optimization of dopant concentration ($Sm^{3+}$: 2−10 mol %; $Gd^{3+}$: 2−8 mol %) yields intense $Mn^{2+}$ emission without detectable $Ln^{3+}$ emission, confirming the occurrence of underlying energy transfer. The resulting ZnSe:$Mn^{2+}$,$Sm^{3+}$ NCs function as effective photoluminescent nanosensors and exhibit remarkable quenching in the presence of $Pb^{2+}$ and $Hg^{2+}$ ions. $Pb^{2+}$ showed a higher quenching constant ($K_{sv}$ = 0.2074 $\mu M^{-1}$) and detection limit (2.51 $\mu$M) compared to $Hg^{2+}$ ($K_{sv}$ = 0.0266 $\mu M^{-1}$; LoD = 6.63 $\mu$M). Quenching arises via combined static and dynamic mechanisms. Selectivity studies indicated that there was negligible interference from competing metal ions; however, simultaneous detection of $Pb^{2+}$ and $Hg^{2+}$ resulted in additive quenching, which limited ion-specific resolution. We note that the nanosensors effectively detected $Pb^{2+}$ and $Hg^{2+}$ ions but lacked selectivity between these ions. The future work should address this challenge by integrating ligands having affinity toward either of the metal ions, i.e., $Pb^{2+}$ or $Hg^{2+}$, or by developing a hybrid sensing modality. These findings establish ZnSe:$Mn^{2+}$,$Sm^{3+}$ NCs as promising candidates for sensitive and selective heavy metal ion detection in complex aqueous environmental matrices.

## 4. EXPERIMENTAL SECTION

### 4.1. Chemicals

These chemicals were sourced from commercial suppliers and utilized as received without any additional purification or modification: the lanthanide acetates, $Ln(CH_3COO)_3{\cdot}6H_2O$ (Ln: Gd and Sm), were prepared from their respective $Ln_2O_3$ oxides (99.99%, Rhodia). Manganese(II) acetate tetrahydrate (≥99%), oleylamine (OLA ≥ 70%), Se powder (Se ≥ 99.5%), 3-mercaptopropionic acid (3-MPA ≥ 99%), 1-dodecanethiol (DDT ≥ 98%), 1-octadecene (ODE ≥ 90%), and sodium hydroxide (NaOH ≥ 97%) were purchased from Sigma-Aldrich (St. Louis, MO, USA). Zinc acetate (≥99%) was sourced from Merck (Darmstadt, Germany). Additionally, oleic acid (OA), chloroform, ethanol, and sucrose were acquired from Labsynth (Diadema, SP, Brazil). Metal salts such as copper acetate ($Cu(ace)_2$), chromium(III) nitrate nonahydrate ($CrN_3O_9{\cdot}9H_2O$), mercury(II) chloride ($HgCl_2$), lead(II) nitrate ($Pb(NO_3)_2$), and ferric chloride hexahydrate ($FeCl_3{\cdot}6H_2O$) were purchased from Sigma-Aldrich (St. Louis, MO, USA).

### 4.2. Synthesis of ZnSe:$Mn^{2+}$,$Ln^{3+}$ NCs

The ZnSe:$Mn^{2+}$,$Ln^{3+}$ ($Ln^{3+}$: $Sm^{3+}$ and $Gd^{3+}$) NCs were synthesized by employing a modified method based on previously reported procedures.[7,39] The synthesis was conducted at an elevated temperature of 280 °C with vigorous magnetic stirring and nitrogen atmosphere utilizing noncoordinating solvent, *i.e.*, 1-octadecene (ODE), along with coordinating solvents and stabilizing agents, including oleic acid (OA), oleylamine (OLA), and 1-dodecanethiol (DDT).[13] Briefly, to synthesize ZnSe:*x*$Mn^{2+}$,*y*$Sm^{3+}$ NCs (*y* = 7 and *x* = 2 mol %), a three-necked flask containing 219.49 mg (1 mmol) of zinc acetate dihydrate, 38.05 mg (0.154 mmol) of manganese acetate dihydrate, 17.74 mg (0.044 mmol) of samarium acetate hexahydrate in 10 mL of ODE, 3 mL of DDT, 3 mL of OLA, and 6 mL of OA was heated to 120 °C for 30 min. The temperature was raised to 300 °C and maintained until a slightly yellow, transparent solution of metal-oleate (Zn-oleate, Ln-oleate, and Mn-oleate) was obtained. Subsequently, Se-precursor, prepared by dissolving 78.96 mg (1 mmol) of selenium powder in a mixture of 3 mL of OLA and 3 mL of 1- DDT under stirring at 35 °C, was injected into the reaction mixture. The reaction was continued for 10 min to facilitate the maximum nucleation and crystal growth of the ZnSe:$Mn^{2+}$,$Sm^{3+}$ NCs. After that, an additional injection of Zn-oleate, prepared by heating 40 mg of $Zn(ace)_2{\cdot}2H_2O$ in 3 mL of ODE and 3 mL of OLA, was performed to passivate the surface defects of NCs, with the reaction maintained for 3 min. After the reaction was completed, the temperature was dropped to 45 °C, and acetone, in a volume twice that of the reaction mixture, was added to precipitate the ZnSe:$Mn^{2+}$,$Sm^{3+}$ NCs. The resultant product was then centrifuged and purified through multiple acetone/chloroform mixture washes to eliminate unreacted precursors and byproducts. The synthesis of other ZnSe:$Mn^{2+}$,$Gd^{3+}$ NCs was performed by the same procedure while adjusting the $Gd^{3+}$ ion concentration to achieve the desired stoichiometry.

### 4.3. Ligand Exchange of ZnSe:$Mn^{2+}$,$Sm^{3+}$ NCs

For metal ion detection, the as-prepared ZnSe:$Mn^{2+}$,$Sm^{3+}$ NCs were rendered water-soluble following the previous procedure.[7,39] Briefly, two homogeneous solutions labeled "A" containing 15 mg of NCs in 3 mL of chloroform and "B" containing 2 mL of 3-MPA in 6 mL of deionized $H_2O_2$ were prepared. The pH of solution B was adjusted to 11 by dropwise addition of NaOH solution (40% w/v) and was subsequently combined with solution A. The resulting biphasic mixture was stirred vigorously at room temperature for 1 h, followed by discarding the organic phase. The NCs in the aqueous phase were precipitated by adding an excess of acetone and then centrifuged at 14,000 rpm for 5 min. The supernatant was decanted to remove the excess 3-MPA, yielding NCs functionalized with 3-MPA. The obtained NCs were resuspended in water containing 3-MPA at pH 11, and the same procedure mentioned above was repeated to ensure maximum ligand replacement of NCs.

### 4.4. Detection of Heavy Metal Ions

The detection studies were performed using ZnSe:$Mn^{2+}$,$Sm^{3+}$ NCs (1 mg/mL) as a sensing platform. Briefly, for $Pb^{2+}$ and $Hg^{2+}$ ion detection, working solutions were prepared and diluted to final concentrations of 1 to 130 $\mu$M and 1 to 210 $\mu$M, respectively, whereas the detection experiments of $Ag^{1+}$, $Co^{2+}$, $Ni^{2+}$, $Cd^{2+}$, $Gd^{3+}$, $Tm^{3+}$, $Yb^{3+}$, and $Er^{3+}$ ions were performed at a final concentration of 50 ppm, for each metal ion. The PL measurements were carried out within 5 min of mixing the NCs with metal ion solutions. The PL spectra and lifetime measurements of ZnSe:$Mn^{2+}$,$Sm^{3+}$ NCs were recorded both without and with different concentrations of metal ions by using an excitation wavelength of 365 nm. Selectivity of nanosensors for $Pb^{2+}$/$Hg^{2+}$ ion detection was systematically evaluated through interference studies with other metal ions, including $Cd^{2+}$, $Co^{2+}$, $Ni^{2+}$, $Cd^{2+}$, $Co^{2+}$, $Ni^{2+}$, and $Ln^{3+}$ ($Gd^{3+}$, and $Tm^{3+}$) across various concentration ranges.

### 4.5. Materials Characterization

X-ray diffraction (XRD) patterns of the ZnSe:$Mn^{2+}$,$Ln^{3+}$ NCs were acquired using a RIGAKU MINIFLEX-II diffractometer, which employed Cu K$\alpha$ radiation ($\lambda$ = 1.5406 Å) and covered a 2$\theta$ range from 0° to 90°. The UV−visible absorption spectra of the QD chloroform suspensions were measured using a UV-2600 UV−visible spectrophotometer from Shimadzu Scientific Instruments Inc., with measurements conducted in quartz cuvettes. For the luminescence spectra and decay curves of the ZnSe:$Mn^{2+}$,$Ln^{3+}$ NCs, recordings were performed at room temperature in a chloroform dispersion at a concentration of 100 mg $L^{-1}$, utilizing a HORIBA Jobin Yvon Fluorolog-3 spectrofluorometer. This instrument incorporates a 450 W xenon lamp and a pulsed xenon flash lamp as excitation sources alongside double grating monochromators, a CCD detector, and a phosphorimeter accessory to enhance measurement performance. The



https://doi.org/10.1021/acsaom.5c00240
ACS Appl. Opt. Mater. 2025, 3, 2067−2077

resulting luminescence data were processed by using FluorEssence software, which facilitates the direct conversion of the acquired data into the Origin software format for subsequent analysis.

XEOL spectra were acquired with an XEOL spectrometer that was newly commissioned at the BM08-XAFS/XRF beamline[43] at SESAME (Synchrotron-light for Experimental Science and Applications in the Middle East). The XEOL spectrometer contains a customized sample environment with multiple entrance windows for the X-ray beam and LASER as well as exit windows to the spectrometer and detectors, all developed in-house and manufactured by 3D printing. The sample environment is equipped with a Basler ace GigE camera and LMVZ540 focusing lens, Kowa, of 5−40 mm focal length. The optical emission from the sample irradiated by a monochromatic X-ray beam is collected through an optical fiber (Ocean Insight) with a 600 mm core diameter, covering the UV−vis and near-IR range (200−11 nm). The optical fiber is connected to a QE Pro-ABS spectrometer (Ocean Insight), which operates in the wavelength range from 200 to 950 nm, with integration times between milliseconds and seconds. The spectrometer is equipped with a Hamamatsu scientific grade back-thinned thermal electrical cooled 1024 × 58 elements CCD array detector.[43]

XAFS (X-ray absorption fine structure) data were measured at the BM08-XAFS/XRF beamline[43] of SESAME, operating at 2.5 GeV in "decay" mode and a maximum electron current of 250 mA. The three ionization chambers for measuring the beam intensity were filled with optimum mixtures of $He/N_2$ gases at a total pressure of 1.0 bar. The XAFS data of Zn K-edge (9659 eV) were measured in transmission mode, whereas Mn K-edge (6539 eV), Gd $L_3$-edge (7243 eV), and Sm $L_3$-edge (6716 eV) were recorded in fluorescence mode, respectively, at room temperature, using a double-crystal Si (111) monochromator. The signals were acquired at the ionization chambers with subsequent amplification by Stanford picoammeters and finally read by data acquisition system (DAQs), and KETEK Silicon Drift Detectors (SDD), using Digital X-ray Processor (DXP), Mercury XIA LLC. The pellets of samples (13 mm diameter) were prepared by applying pressure (less than 2 tons) on the homogeneous mixture of the finely ground sample and polyvinylpyrrolidone (PVP) powder.

## ■ ASSOCIATED CONTENT

### Supporting Information

The Supporting Information is available free of charge at https://pubs.acs.org/doi/10.1021/acsaom.5c00240.

XRD patterns; XANES spectra; photoluminescence quenching spectra; Stern−Volmer equations (PDF)

Real-time photoluminescence quenching video S1 (MP4)

## ■ AUTHOR INFORMATION


### Corresponding Authors

**Zahid U. Khan** − *Research Centre for Greenhouse Gas Innovation, University of São Paulo (USP), 05508-030 São Paulo, SP, Brazil; Institute of Chemistry, University of São Paulo (USP), 05508-000 São Paulo, SP, Brazil;* orcid.org/0000-0003-1529-0832; Email: zahid@iq.usp.br

**Muhammad Abdullah Khan** − *Renewable Energy Advancement Laboratory, Department of Environmental Sciences, Quaid-i-Azam University, 15320 Islamabad, Pakistan;* orcid.org/0000-0003-2500-8036; Email: makhan@qau.edu.pk

### Authors

**Iram Gul** − *Renewable Energy Advancement Laboratory, Department of Environmental Sciences, Quaid-i-Azam University, 15320 Islamabad, Pakistan; Research Centre for Greenhouse Gas Innovation, University of São Paulo (USP), 05508-030 São Paulo, SP, Brazil*

**Sammra Galani** − *Renewable Energy Advancement Laboratory, Department of Environmental Sciences, Quaid-i-Azam University, 15320 Islamabad, Pakistan*

**Subul Huda** − *Renewable Energy Advancement Laboratory, Department of Environmental Sciences, Quaid-i-Azam University, 15320 Islamabad, Pakistan;* orcid.org/0009-0004-7724-0798

**Latif U. Khan** − *Institute of Chemistry, University of São Paulo (USP), 05508-000 São Paulo, SP, Brazil; Synchrotron-light for Experimental Science and Applications in the Middle East (SESAME), Allan 19252, Jordan;* orcid.org/0000-0002-3535-7099

**Hassan K. Juwhari** − *Physics Department, School of Science, University of Jordan, Amman 11942, Jordan*

**Ali Hyder** − *Institute of Chemistry, University of São Paulo (USP), 05508-000 São Paulo, SP, Brazil*

**Hermi F. Brito** − *Institute of Chemistry, University of São Paulo (USP), 05508-000 São Paulo, SP, Brazil;* orcid.org/0000-0002-9876-4441

**Muhammad Zaheer** − *Department of Chemistry and Chemical Engineering, Syed Babar Ali School of Science and Engineering, Lahore University of Management Sciences (LUMS), Lahore 54792, Pakistan;* orcid.org/0000-0003-2389-4396

Complete contact information is available at: https://pubs.acs.org/10.1021/acsaom.5c00240



### Funding

The Article Processing Charge for the publication of this research was funded by the Coordenacao de Aperfeicoamento de Pessoal de Nivel Superior (CAPES), Brazil (ROR identifier: 00x0ma614).

### Notes

The authors declare no competing financial interest.

## ■ ACKNOWLEDGMENTS

The author (Latif U. Khan) acknowledges the financial support from the International Atomic Energy Agency (IAEA) for the XEOL experimental setup at the end station of BM08-XAFS/XRF beamline, SESAME synchrotron light source, and the Royal Society of Chemistry Inclusion and Diversity Fund (RSC). We gratefully acknowledge the financial support provided by the Fundação de Amparo à Pesquisa do Estado de São Paulo (FAPESP), under grant numbers: 2021/00356-6 (Zahid U. Khan) and 2021/08111-2 (Hermi F. Brito) and CNPq (308872/2022-3).


## ■ REFERENCES


(1) Goyal, R. K.; Maharaj, S.; Kumar, P.; Chandrasekhar, M. Exploring Quantum Materials and Applications: A Review. *J. Mater. Sci. Mater. Eng.* **2025**, *20* (1), 4.

(2) García de Arquer, F. P.; Talapin, D. V.; Klimov, V. I.; Arakawa, Y.; Bayer, M.; Sargent, E. H. Semiconductor Quantum Dots: Technological Progress and Future Challenges. *Science* **2021**, *373* (6555), No. eazz8541.

(3) Jin, L.; Selopal, G. S.; Sun, X. W.; Rosei, F. Core-Shell Colloidal Quantum Dots for Energy Conversion. *Adv. Energy Mater.* **2025**, *15*, 2403574.

(4) Cao, M.; Zhao, X.; Gong, X. Achieving High-Efficiency Large-Area Luminescent Solar Concentrators. *JACS Au* **2023**, *3* (1), 25−35.

(5) Kargozar, S.; Hoseini, S. J.; Milan, P. B.; Hooshmand, S.; Kim, H. W.; Mozafari, M. Quantum Dots: A Review from Concept to Clinic. *Biotechnol. J.* **2020**, *15* (12), 1−18.
(6) Sahu, A.; Kumar, D. Core-Shell Quantum Dots: A Review on Classification, Materials, Application, and Theoretical Modeling. *J. Alloys Compd.* **2022**, *924*, No. 166508.
(7) Gidlund, M.; Khan, Z. U.; Uchiyama, M. K.; Khan, L. U.; Ramos-Sanchez, E. M.; Reis, L. C.; Nakamura, M.; Goto, H.; de Souza, A. O.; Araki, K.; Brito, H. F. Orange-Emitting ZnSe:$Mn^{2+}$ Quantum Dots as Nanoprobes for Macrophages. *ACS Appl. Nano Mater.* **2020**, *3* (10), 10399−10410.
(8) Khan, Z. U.; Khan, L. U.; Brito, H. F.; Gidlund, M.; Malta, O. L.; Di Mascio, P. Colloidal Quantum Dots as an Emerging Vast Platform and Versatile Sensitizer for Singlet Molecular Oxygen Generation. *ACS Omega* **2023**, *8* (38), 34328−34353.
(9) Khan, Z. U.; Khan, L. U.; Uchiyama, M. K.; Prado, F. M.; Faria, R. L.; Costa, I. F.; Miyamoto, S.; Araki, K.; Gidlund, M.; Brito, H. F.; Di Mascio, P. Singlet Molecular Oxygen Generation via Unexpected Emission Color-Tunable CdSe/ZnS Nanocrystals for Applications in Photodynamic Therapy. *ACS Appl. Nano Mater.* **2023**, *6* (5), 3767−3780.
(10) Khan, Z. U.; Uchiyama, M. K.; Khan, L. U.; Araki, K.; Goto, H.; Felinto, M. C. F. C.; De Souza, A. O.; De Brito, H. F.; Gidlund, M. Wide Visible-Range Activatable Fluorescence ZnSe:$Eu^{3+}$/$Mn^{2+}$@ZnS Quantum Dots: Local Atomic Structure Order and Application as a Nanoprobe for Bioimaging. *J. Mater. Chem. B* **2022**, *10* (2), 247−261.
(11) Ratnesh, R. K.; Mehata, M. S. Investigation of Biocompatible and Protein Sensitive Highly Luminescent Quantum Dots/Nanocrystals of CdSe, CdSe/ZnS and CdSe/CdS. *Spectrochim. Acta - Part A Mol. Biomol. Spectrosc.* **2017**, *179*, 201−210.
(12) Lu, X.; Zhang, J.; Xie, Y. N.; Zhang, X.; Jiang, X.; Hou, X.; Wu, P. Ratiometric Phosphorescent Probe for Thallium in Serum, Water, and Soil Samples Based on Long-Lived, Spectrally Resolved, Mn-Doped ZnSe Quantum Dots and Carbon Dots. *Anal. Chem.* **2018**, *90* (4), 2939−2945.
(13) Yang, X.; Pu, C.; Qin, H.; Liu, S.; Xu, Z.; Peng, X. Temperature- A Nd $Mn^{2+}$ Concentration-Dependent Emission Properties of $Mn^{2+}$-Doped ZnSe Nanocrystals. *J. Am. Chem. Soc.* **2019**, *141* (6), 2288−2298.
(14) Yang, Y.; Mao, G.; Ji, X.; He, Z. DNA-Templated Quantum Dots and Their Applications in Biosensors, Bioimaging, and Therapy. *J. Mater. Chem. B* **2020**, *8* (1), 9−17.
(15) Bhatia, D.; Arumugam, S.; Nasilowski, M.; Joshi, H.; Wunder, C.; Chambon, V.; Prakash, V.; Grazon, C.; Nadal, B.; Maiti, P. K.; Johannes, L.; Dubertret, B.; Krishnan, Y. Quantum Dot-Loaded Monofunctionalized DNA Icosahedra for Single-Particle Tracking of Endocytic Pathways. *Nat. Nanotechnol.* **2016**, *11* (12), 1112−1119.
(16) Lakowicz, J. R. *Principles of Fluorescence Spectroscopy*; Springer, 2006. DOI: 10.1007/978-0-387-46312-4.
(17) Santra, S.; Dutta, S.; Adalder, A. Advances in the Ratiometric Combination of Quantum Dots for Their Use in Sensing Applications. *Mater. Adv.* **2023**, *4* (20), 4646−4664.
(18) Hofman, E.; Khammang, A.; Wright, J. T.; Li, Z.-J.; McLaughlin, P. F.; Davis, A. H.; Franck, J. M.; Chakraborty, A.; Meulenberg, R. W.; Zheng, W. Decoupling and Coupling of the Host−Dopant Interaction by Manipulating Dopant Movement in Core/Shell Quantum Dots. *J. Phys. Chem. Lett.* **2020**, *11* (15), 5992−5999.
(19) Guo, X.; Huang, J.; Wei, Y.; Zeng, Q.; Wang, L. Fast and Selective Detection of Mercury Ions in Environmental Water by Paper-Based Fluorescent Sensor Using Boronic Acid Functionalized $MoS_2$ Quantum Dots. *J. Hazard. Mater.* **2020**, *381*, 120969.
(20) Bolisetty, S.; Peydayesh, M.; Mezzenga, R. Sustainable Technologies for Water Purification from Heavy Metals: Review and Analysis. *Chem. Soc. Rev.* **2019**, *48* (2), 463−487.
(21) Mukherjee, S.; Bhattacharyya, S.; Ghosh, K.; Pal, S.; Halder, A.; Naseri, M.; Mohammadniaei, M.; Sarkar, S.; Ghosh, A.; Sun, Y.; Bhattacharyya, N. Sensory Development for Heavy Metal Detection: A Review on Translation from Conventional Analysis to Field-Portable Sensor. *Trends Food Sci. Technol.* **2021**, *109*, 674−689.
(22) Hu, Q.; Yang, G.; Zhao, Y.; Yin, J. Determination of Copper, Nickel, Cobalt, Silver, Lead, Cadmium, and Mercury Ions in Water by Solid-Phase Extraction and the RP-HPLC with UV-Vis Detection. *Anal. Bioanal. Chem.* **2003**, *375* (6), 831−835.
(23) Renu, K.; Chakraborty, R.; Myakala, H.; Koti, R.; Famurewa, A. C.; Madhyastha, H.; Vellingiri, B.; George, A.; Valsala Gopalakrishnan, A. Molecular Mechanism of Heavy Metals (Lead, Chromium, Arsenic, Mercury, Nickel and Cadmium) - Induced Hepatotoxicity−A Review. *Chemosphere.* **2021**, *271*, No. 129735.
(24) Ravipati, E. S.; Mahajan, N. N.; Sharma, S.; Hatware, K. V.; Patil, K. The Toxicological Effects of Lead and Its Analytical Trends: An Update from 2000 to 2018. *Crit. Rev. Anal. Chem.* **2021**, *51* (1), 87−102.
(25) Kumar, A.; Kumar, A.; Cabral-Pinto, M.; Chaturvedi, A. K.; Shabnam, A. A.; Subrahmanyam, G.; Mondal, R.; Gupta, D. K.; Malyan, S. K.; Kumar, S. S.; Khan, S. A.; Yadav, K. K. Lead Toxicity: Health Hazards, Influence on Food Chain, and Sustainable Remediation Approaches. *International Journal of Environmental Research and Public Health.* **2020**, *17* (7), 2179.
(26) Sardans, J.; Montes, F.; Peñuelas, J. Determination of As, Cd, Cu, Hg and Pb in Biological Samples by Modern Electrothermal Atomic Absorption Spectrometry. *Spectrochim. Acta - Part B At. Spectrosc.* **2010**, *65* (2), 97−112.
(27) He, Q.; Miller, E. W.; Wong, A. P.; Chang, C. J. A Selective Fluorescent Sensor for Detecting Lead in Living Cells. *J. Am. Chem. Soc.* **2006**, *128* (29), 9316−9317.
(28) Li, X.; Wang, G.; Ding, X.; Chen, Y.; Gou, Y.; Lu, Y. A "Turn-on" Fluorescent Sensor for Detection of $Pb^{2+}$ Based on Graphene Oxide and G-Quadruplex DNA. *Phys. Chem. Chem. Phys.* **2013**, *15* (31), 12800−12804.
(29) Wu, P.; Yan, X. P. Doped Quantum Dots for Chemo/Biosensing and Bioimaging. *Chem. Soc. Rev.* **2013**, *42* (12), 5489−5521.
(30) Anand, T.; Sivaraman, G.; Mahesh, A.; Chellappa, D. Aminoquinoline Based Highly Sensitive Fluorescent Sensor for Lead(II) and Aluminum(III) and Its Application in Live Cell Imaging. *Anal. Chim. Acta* **2015**, *853* (C), 596−601.
(31) Bera, D.; Qian, L.; Tseng, T. K.; Holloway, P. H. Quantum Dots and Their Multimodal Applications: A Review. *Materials (Basel).* **2010**, *3* (4), 2260−2345.
(32) Petryayeva, E.; Algar, W. R.; Medintz, I. L. Quantum Dots in Bioanalysis: A Review of Applications across Various Platforms for Fluorescence Spectroscopy and Imaging. *Appl. Spectrosc.* **2013**, *67* (3), 215−252.
(33) Mabrouk, S.; Rinnert, H.; Balan, L.; Jasniewski, J.; Medjahdi, G.; Ben Chaabane, R.; Schneider, R. Aqueous Synthesis of Core/Shell/Shell ZnSeS/Cu:ZnS/ZnS Quantum Dots and Their Use as a Probe for the Selective Photoluminescent Detection of $Pb^{2+}$ in Water. *J. Photochem. Photobiol. A Chem.* **2022**, *431*, No. 114050.
(34) Sharma, V.; Mehata, M. S. Synthesis of Photoactivated Highly Fluorescent $Mn^{2+}$-Doped ZnSe Quantum Dots as Effective Lead Sensor in Drinking Water. *Mater. Res. Bull.* **2021**, *134*, No. 111121.
(35) Devaiah Chonamada, T.; Sharma, B.; Nagesh, J.; Shibu, A.; Das, S.; Bramhaiah, K.; Rajendar, N.; John, N. S.; Santra, P. K. Origin of Luminescence-Based Detection of Metal Ions by Mn−Doped ZnS Quantum Dots. *ChemistrySelect* **2019**, *4* (46), 13551−13557.
(36) Zou, W.-S.; Deng, M.-Y.; Wang, Y.-Q.; Zhao, X.; Li, W.-H.; Huang, X.-H. Alginate Capped and Manganese Doped ZnS Quantum Dots as a Phosphorescent Probe for Time-Resolved Detection of Copper(II). *Microchim. Acta* **2019**, *186* (1), 41.
(37) Gu, X.; Li, M.; Yan, Y.; Miao, J. Construction of a Fluorescence Switch Sensor of Mn Doped AgInS2 Quantum Dots for the Detection of Fe (III) and Ascorbic Acid. *Spectrochim. Acta Part A Mol. Biomol. Spectrosc.* **2024**, *321*, No. 124709.
(38) Byers, H. L.; McHenry, L. J.; Grundl, T. J. XRF Techniques to Quantify Heavy Metals in Vegetables at Low Detection Limits. *Food Chem. X* **2019**, *1*, No. 100001.

(39) Khan, Z. U.; Khan, L. U.; Uchiyama, M. K.; Prado, F. M.; Faria, R. L.; Costa, I. F.; Miyamoto, S.; Araki, K.; Gidlund, M.; Brito, H. F.; Di Mascio, P. Singlet Molecular Oxygen Generation via Unexpected Emission Color-Tunable CdSe/ZnS Nanocrystals for Applications in Photodynamic Therapy. *ACS Appl. Nano Mater.* **2023**, *6* (5), 3767−3780.
(40) Newville, M. Larch: An Analysis Package for XAFS and Related Spectroscopies. *J. Phys. Conf. Ser.* **2013**, *430* (1), No. 012007.
(41) Khan, L. U.; Khan, Z. U.; Blois, L.; Tabassam, L.; Brito, H. F.; Figueroa, S. J. A. Strategy to Probe the Local Atomic Structure of Luminescent Rare Earth Complexes by X-Ray Absorption Near-Edge Spectroscopy Simulation Using a Machine Learning-Based PyFitIt Approach. *Inorg. Chem.* **2023**, *62* (6), 2738−2750.
(42) Gul, I.; Khan, Z. U.; Khan, M. A.; Cabrera-Pasca, G. A.; AlZubi, R. I.; Figueroa, S. J. A.; Brito, H. F.; Khan, L. U. $Ln^{3+}$-Ion-Mediated Enhancement in UV/X-Ray-Induced Optical Emission from $Mn^{2+}$-Doped ZnSe Nanocrystals. *Nanoscale* **2025**, *17*, 15393.
(43) Khan, L. U.; Khan, Z. U.; Alzubi, R. I.; Umer, M. A.; Juwhari, K.; Harfouche, M.; Brito, H. F. Tracking Coordination Environment and Optoelectronic Structure of $Eu^{3+}$ and $Sm^{3+}$ Sites via X-Ray Absorption Spectroscopy and X-Ray Excited Optical Luminescence. *Mater. Today Proc.* **2024**, 1−8.
(44) Xu, M.; Wang, X.; Liu, X. Detection of Heavy Metal Ions by Ratiometric Photoelectric Sensor. *J. Agric. Food Chem.* **2022**, *70* (37), 11468−11480.
(45) Wu, P.; Zhao, T.; Wang, S.; Hou, X. Semicondutor Quantum Dots-Based Metal Ion Probes. *Nanoscale* **2014**, *6* (1), 43−64.
(46) Labeb, M.; Sakr, A.-H.; Soliman, M.; Abdel-Fattah, T. M.; Ebrahim, S. Effect of Capping Agent on Selectivity and Sensitivity of CdTe Quantum Dots Optical Sensor for Detection of Mercury Ions. *Opt. Mater. (Amst).* **2018**, *79*, 331−335.
(47) Lou, Y.; Zhao, Y.; Chen, J.; Zhu, J.-J. Metal Ions Optical Sensing by Semiconductor Quantum Dots. *J. Mater. Chem. C* **2014**, *2* (4), 595−613.
(48) Ke, J.; Li, X.; Zhao, Q.; Hou, Y.; Chen, J. Ultrasensitive Quantum Dot Fluorescence Quenching Assay for Selective Detection of Mercury Ions in Drinking Water. *Sci. Rep.* **2014**, *4*, 4−9.
(49) Farahmandzadeh, F.; Kermanshahian, K.; Molahosseini, E.; Molaei, M. Efficient Mercury Ion Detection in Water: CdTe/CdS/ZnS Quantum Dots as a Simple, Sensitive, and Rapid Fluorescence Sensor. *J. Fluoresc.* **2025**, *35*, 4829.
(50) Parani, S.; Tsolekile, N.; May, B. M. M.; Pandiyan, K.; Oluwafemi, O. S. Mn-Doped ZnSe Quantum Dots as Fluorimetric Mercury Sensor. *Nonmagnetic Magn. Quantum Dots* **2018**.
(51) Xue, T.; Shi, Y.; Guo, J.; Guo, M.; Yan, Y. Preparation of $AgInS_2$ Quantum Dots and Their Application for $Pb^{2+}$ Detection Based on Fluorescence Quenching Effect. *Vacuum* **2021**, *193*, No. 110514.
(52) Zhou, J.; Li, B.; Qi, A.; Shi, Y.; Qi, J.; Xu, H.; Chen, L. ZnSe Quantum Dot Based Ion Imprinting Technology for Fluorescence Detecting Cadmium and Lead Ions on a Three-Dimensional Rotary Paper-Based Microfluidic Chip. *Sensors Actuators B Chem.* **2020**, *305*, No. 127462.
(53) Farahmandzadeh, F.; Salehi, S.; Molaei, M.; Fallah, H.; Nejadshafiee, V. CdS Semiconductor Quantum Dots; Facile Synthesis, Application as Off Fluorescent Sensor for Detection of Lead ($Pb^{2+}$) Ions and Catalyst for Degradation of Dyes from Water. *J. Fluoresc.* **2023**, *33* (4), 1515−1524.
(54) Ajroud, M.; Abdella, F. I. A.; Alanazi, T. Y. A.; Helaoui, M.; Boudriga, S. Exploring the Probing Capacities of MSA Capped CdTe Semiconductor Quantum Dots as Optical Chemsensors via Analytical and Isotherms Modeling for Selective $Hg^{2+}$ Detection. *Appl. Water Sci.* **2024**, *14* (2), 15.
(55) Li, H.; Wang, W.; Wang, Z.; Lv, Q.; Bai, H.; Zhang, Q. Analyte-Enhanced Photocatalytic Activity of CdSe/ZnS Quantum Dots for Paper-Based Colorimetric Sensing of $Hg^{2+}$ under Visible Light. *Microchem. J.* **2021**, *164*, No. 106037.
(56) Chu, H.; Yao, D.; Chen, J.; Yu, M.; Su, L. Double-Emission Ratiometric Fluorescent Sensors Composed of Rare-Earth-Doped ZnS Quantum Dots for $Hg^{2+}$ Detection. *ACS Omega* **2020**, *5* (16), 9558−9565.
(57) Cai, Z.; Shi, B.; Zhao, L.; Ma, M. Ultrasensitive and Rapid Lead Sensing in Water Based on Environmental Friendly and High Luminescent L-Glutathione-Capped-ZnSe Quantum Dots. *Spectrochim. Acta - Part A Mol. Biomol. Spectrosc.* **2012**, *97*, 909−914.




https://doi.org/10.1021/acsaom.5c00240
ACS Appl. Opt. Mater. 2025, 3, 2067−2077